Check for updates

Optically induced charge separation at the naphthalenediimide–phenothiazine interface

Thomas Trepl, [ID] [a] Renan G. de Assis, [ID] [b] Christine M. Isborn, [ID] [c] Thiago B. de Queiroz [ID] [b] and Stephan Kümmel [ID] *[a]

Naphthalenediimide (NDI) is stable under ambient air and an efficient electron acceptor due to its high electron affinity. Phenothiazine derivatives are paradigm electron donors due to their relatively low oxidation potentials and cations of high stability. Combining these two system classes therefore appears as a promising strategy for obtaining a material with attractive optoelectronic properties. We here investigate molecular models of π-coupled junctions of *N*,*N*′-bis[3-(triethoxysilyl)propyl]-1,4,5,8-naphthalenediimide (NDI-silane) and 3,7-di-*t*-butylphenothiazine (TBP) using time-dependent density functional theory. We calculate the electronic excitations for systems with frozen nuclei, and in a second step also investigate the influence that the dynamics of the nuclei has on the electronic excitations. We find optically active excitations around 1.5 eV that are associated with a charge transfer at the interface. We further calculate the electronic couplings between the states that are the most relevant ones for charge separation. Our findings can be seen as indicators for these materials' suitability for photovoltaic applications. First experimental results are in line with the theoretical conclusions.

1 Introduction

During the past years, the quest for sustainable sources of energy has led to remarkable advances in the development of photovoltaic materials.[1] Donor–acceptor molecular systems for photoinduced charge separation hold the promise to become key actors in clean energy generation, particularly in the context of organic photovoltaic devices.[2–5] Traditionally, fullerene derivatives, such as PCBM-60 and PCBM-70, have been used in combination with low-bandgap polymers to form the active layers of organic photovoltaic materials.[6–8] However, non-fullerenes are finding increasing interest as they can offer important advantages, *e.g.*, in terms of light absorption, level alignment, and possibly structural stability.[9–19]

Time-dependent density functional theory (TDDFT) is ideally suited for obtaining insight into the electronic structure and excitations of molecules and solids, and can thus support the search for new energy converting materials.[20–25] With modern functionals, such as optimally-tuned range-separated hybrids, the limitations of traditional semilocal functionals in the accuracy of the prediction of relative electronic levels, band

gaps, and charge-transfer excitations can be overcome.[22,26–29] Here, we employ DFT and TDDFT to check a combination of materials for potential suitability in photovoltaic devices. Naphthalenediimide (NDI) is an electron-deficient ring system that has been proposed as a backbone or skeleton for electron acceptor applications due to its relatively high electron affinity and ambient air stability.[30–33] It is chemically flexible and can be functionalized with siloxyl groups to permit sol–gel chemistry in device fabrication,[34,35] and can be attached to electron withdrawing groups to manipulate its electronic properties.[36] On the other hand, phenothiazine dyes are excellent light absorbers, good electron donors and also chemically flexible.[37–41] Consequently, the combination of these materials holds potential for the development of efficient and durable photoinduced charge-separating devices.

In this article, we investigate the combination of 3,7-di-*t*-butylphenothiazine (TBP) as a donor molecule and *N*,*N*′-bis[3-(triethoxysilyl)propyl]-1,4,5,8-naphthalenediimide (NDI-silane) as an acceptor molecule. Fig. 1 shows a sketch of the chemical structure of these molecules.

From these building blocks we construct molecular models that allow us to investigate the excited state properties of the donor–acceptor interface with the help of (TD)DFT.[42,43] We explore possible charge-separation pathways and investigate the influence of nuclear motion on the excited-state properties. The calculations are complemented by experiments that demonstrate the successful synthesis of these molecular systems and the first steps in their spectroscopic characterization.

[a] Theoretical Physics IV, University of Bayreuth, 95440 Bayreuth, Germany. E-mail: stephan.kuemmel@uni-bayreuth.de

[b] Center for Natural and Human Sciences, Federal University of ABC, 09210-580 Santo André-SP, Brazil. E-mail: thiago.branquinho@ufabc.edu.br

[c] Department of Chemistry and Biochemistry, University of California Merced, Merced, California 95343, USA
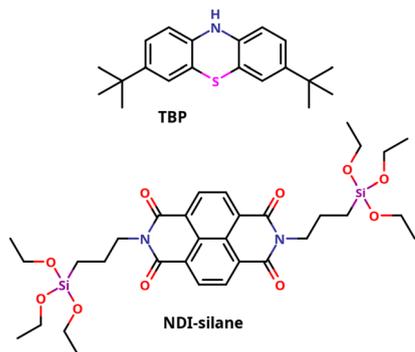
24806 | *Phys. Chem. Chem. Phys.*, 2025, **27**, 24806–24815

This journal is © the Owner Societies 2025

Fig. 1 2D representation of the TBP and NDI-silane molecules.

2 Results and discussions

2.1 The interface models – 1 × 1, 2 × 2, and 3 × 3 TBP/NDI-silane molecular systems

Our aim is the prediction of possible material properties from first principles. DFT and TDDFT allow for the quantitative prediction of both the structure and the excitations of multi-chromophoric systems and are therefore our methods of choice.

We modeled three π-stacked interfaces for the following purposes: (i) By 1-TBP–1-NDI-silane we denote a 1 × 1 molecular system, *i.e.*, a combination of one TBP with one NDI-silane molecule. We use this dimer system to estimate the binding energy between the molecules and to predict, *a priori*, their roles as donor and acceptor entities from their ionization energies and electron affinities. (ii) The 2-TBP–2-NDI-silane is a 2 × 2 molecular system. We use it to investigate the excited states, especially how they are influenced by the motion of the atomic nuclei which we take into account *via* DFT-based *ab initio* molecular dynamics. (iii) The 3-TBP–3-NDI-silane is a 3 × 3 molecular system. It is the largest model that we study here in order to explore the properties of the excitations and possible charge-transfer at the TBP–NDI-silane interface.

For the geometry optimization of the model interfaces, the single molecules are optimized individually and placed in an arbitrary plane-to-plane orientation with a distance of about 4 Å, which is the typical range in which dispersive interactions are significant for these conjugated molecules.[44] Then, DFT-based geometry optimizations are performed. For the latter we use the M06-2X[45] functional because it has been shown to accurately predict intermolecular distances and binding energies of similar molecular systems.[44]

For the 1-TBP–1-NDI-silane system, the plane-to-plane equilibrium distance between the molecules is 3.18 Å and their binding energy is −21.3 kcal mol^{-1} (calculated with the M06-2X functional[45] and 6-311++G** basis set). This value reveals significant coupling between the molecules. For comparison, Kumar *et al.* have investigated the charge-transfer performance of several combinations of π-stacked donor–acceptor systems and found substantial binding and frontier orbital congruence for the pyrene–NDI pair.[46] For this system, the optimal interplanar distance is about 3.35 Å and the binding energy is about −18 kcal mol^{-1}.[44]

For the calculation of charge-transfer excitations with TDDFT, care must be taken. Local or semi-local approximations yield the computationally most efficient exchange–correlation functionals, but they systematically underestimate charge-transfer excitation energies. Therefore, one typically resorts to range-separated hybrid functionals, potentially in combination with optimal tuning of the range-separation parameter.[26] We here use the range-separated hybrid functional ωPBE[47] with a range-separation parameter determined by optimal tuning according to the $J2$ criterion.[48] In this procedure, the exchange term of the functional is split into short-range and long-range parts. The short-range component is represented by a semi-local approximation while the long-range component is represented by the exact Fock exchange. The range-separation parameter ω is chosen such that the frontier eigenvalues are as close as possible to the ionization potential and the electron affinity as determined from total energy differences. This is achieved by minimizing the function $J^2(\omega) = (\varepsilon_{\text{HOMO}}^N(\omega) + \text{IP}^N(\omega))^2 + (\varepsilon_{\text{HOMO}}^{N+1}(\omega) + \text{IP}^{N+1}(\omega))^2$, where N is the number of electrons of the molecule's most stable oxidation state. This strategy of optimal tuning, and also variants of it, has proven its reliability in many cases.[21,22,25,27,28] However, it comes at an unavoidable computational cost. Our largest interface model, the 3 × 3 molecular system consisting of 417 atoms with 1584 electrons, is at the upper end of the system size that can reasonably be studied with this relatively high level of accuracy.

Table 1 lists the optimally tuned ω, generalized Kohn–Sham orbital eigenvalues, ionization energies, and $J(\omega)$ (where $J = \sqrt{J^2}$) evaluated at ω_{opt} for the optimized geometries. While the optimal range-separation parameter is system-dependent, especially in systems in which the extension of the effective conjugation depends on the system size, we find that ω_{opt} is similar for both isolated molecules. This is a reassuring result because it indicates that also the combined systems, *i.e.*, the interface models, can be reasonably well described with one common value of ω_{opt}. The reliability of the optimal tuning is confirmed by the low values that we find for $J(\omega_{\text{opt}})$ when we do the tuning for the interface models, *cf.* Table 1.

We note that the ionization energy and electron affinity of the NDI-silane are about 8.61 eV and 1.80 eV, respectively. For TBP, we find the values 6.55 and −1.23 eV. The negative value of the electron affinity, which corresponds to a positive LUMO eigenvalue, only indicates that TBP does not accept an additional electron, in line with the donor character of the molecule, but the value itself does not have physical meaning. It just

Table 1 Optimal ω, HOMO eigenvalues (ε), ionization energies, and $J(\omega_{\text{opt}})$ for the structures as calculated with optimally tuning

System	ω_{opt} ($10^{-3}\ a_0^{-1}$)	$\varepsilon_{\text{HOMO}}^N$ (eV)	IP^N (eV)	$\varepsilon_{\text{HOMO}}^{N+1}$ (eV)	IP^{N+1} (eV)	$J(\omega_{\text{opt}})$ (meV)
TBP	209	−6.54	6.55	1.22	−1.23	14
NDI-silane	213	−8.62	8.61	−1.79	1.80	21
1-TBP–1-NDI-silane	173	−6.06	6.04	−1.65	1.68	33
2-TBP–2-NDI-silane	136	−5.67	5.71	−2.35	2.32	50
3-TBP–3-NDI-silane	131	−5.67	5.68	−2.37	2.37	9

This journal is © the Owner Societies 2025

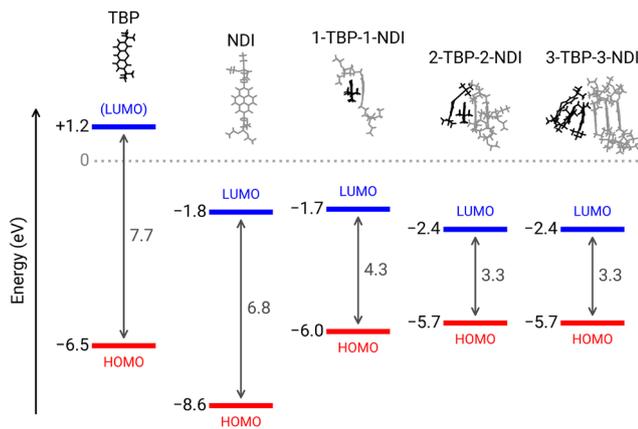*Phys. Chem. Chem. Phys.*, 2025, **27**, 24806–24815 | **24807**

Fig. 2 Energy level diagram (based on the generalized Kohn–Sham eigenvalues) of TBP and NDI-silane as single molecules and their interfaces. From left to right, we display TBP, NDI-silane, 1-TBP–1-NDI-silane, 2-TBP–2-NDI-silane, and 3-TBP–3-NDI-silane. For each structure we display the optimized geometry (TBPs: black, NDI-silanes: gray), the eigenvalue of the lowest unoccupied molecular orbital (LUMO) in blue, the eigenvalue of the highest occupied molecular orbital (HOMO) in red, and the value for the HOMO–LUMO gap. The vacuum level is indicated by a vertical dotted line. The LUMO eigenvalue reported for TBP is the value that we find with the basis set 6-31G**. The positive eigenvalue does not have much physical meaning, as discussed in the main text, therefore it is set in parentheses.

results from the use of a finite, localized basis set. The relevant eigenvalues show a typical donor–acceptor "cascade" alignment, as illustrated in Fig. 2. For the coupled 1-TBP–1-NDI-silane the ionization energy is close to that of the isolated donor (6.55 eV) and the electron affinity is close to that of the isolated acceptor (1.80 eV). This shows that also in the combined system, the distinct donor and acceptor properties are retained. Similar observations are made for the 2-TBP–2-NDI-silane and 3-TBP–3-NDI-silane systems, but there one sees an additional narrowing of the gap from 4.36 eV to 3.39 eV and 3.31 eV. The onset of the saturation of the gap confirms the consistency of our multimolecular approach. Altogether, these results confirm that TBP–NDI-silane is a promising model structure for photoinduced charge separation, which motivated us to proceed further with its evaluation.

2.2 Electronic excitations in the 3-TBP–3-NDI-silane interface

Within our set of molecular models, the 3×3 system comes closest to capturing the properties of an interface, therefore we start by presenting these results. The geometry optimization of the 3×3 systems leads to a stable configuration in which all 6 molecules are bound to each other by π-stacking of the molecules' aromatic rings. Table 2 reports the energies and oscillator strengths for the lowest eight singlet excitations. For completeness we also calculated the lowest-lying triplet excitation energies. They are found at 1.19 eV, 1.70 eV, 1.77 eV, 1.99 eV, 2.05 eV, 2.21 eV, 2.25 eV, and 2.28 eV. These states are not directly optically accessible, and we see that the triplet energies are not in the energetic range that could be relevant for fission of the lowest singlet. As triplet states are therefore not expected to

Table 2 Excitation energies, oscillator strengths, and exciton binding energies for the first eight excited states of the 3-TBP–3-NDI-silane interface model

State	Excitation energy (eV)	O.S.	Exciton binding energy (eV)
S1	1.47	0.1039	1.66
S2	1.73	0.0285	1.40
S3	1.78	0.0011	1.35
S4	2.05	0.0004	1.08
S5	2.25	0.0001	0.88
S6	2.42	0.0003	0.71
S7	2.46	0.0008	0.68
S8	2.52	0.0109	0.61

participate in the initial photophysics of the system, the subsequent discussion will focus on the singlet excitations.

Several important insights emerge from the singlet excitation data. First, the lowest excitation appears at 1.47 eV. This is close to the value 1.4 eV that is considered as the optimal gap for single junction organic solar cells.[49] Second, the S1 excitation carries oscillator strength, *i.e.*, it can be directly accessed optically. Third, several further excitations appear within a few tenths of an eV above the S1 energy. Their oscillator strengths vary, but are lower than that of S1. Finally, S8 appears at 2.52 eV, *i.e.*, still in the visible range.

Further understanding of these findings can be gained by analyzing the excitations in terms of their difference density, *i.e.*, the difference between the excited-state density and the ground-state density. Fig. 3 depicts the difference densities for S1–S8 by visualizing regions where the electron density in the excited state is higher than the ground-state density in blue, and regions where it is lower in red, *i.e.*, red regions can be interpreted as "holes".

The plots show that all of the excitations are associated with a (partial) charge-transfer from the region of the TBP molecules on the left to the region of the NDI-silane molecules on the right. The extension of the charge transfer is different in the different excitations. The difference densities of S1 and S8 show a charge transfer from the innermost TBP molecule to the innermost NDI-silane molecule, *i.e.*, the particle and hole densities are directly neighboring at the interface and the charge transfer is thus relatively short ranged. In S2, the charge separation is larger as the hole density is still on the TBP molecule at the interface, but the particle density is mostly on the second, middle NDI-silane molecule. In S3, the situation is reversed, *i.e.*, the particle density is on the NDI-silane molecule at the interface, but the hole density is on the second, middle TBP molecule. In S4, both particle and hole density have moved to the second layer, and for the yet higher excitations these trends continue, with particle and hole densities then also involving the outermost molecules and delocalizing over several molecules within the donor or acceptor region, respectively.

The typical situation that one thinks about in organic solar cells[20,50] is that light is absorbed *via* an optically active non-charge transfer excitation. The excitation energy then goes over to a (dark) charge-transfer state, and further steps then lead to the charge-separated state and the collection of charges at the
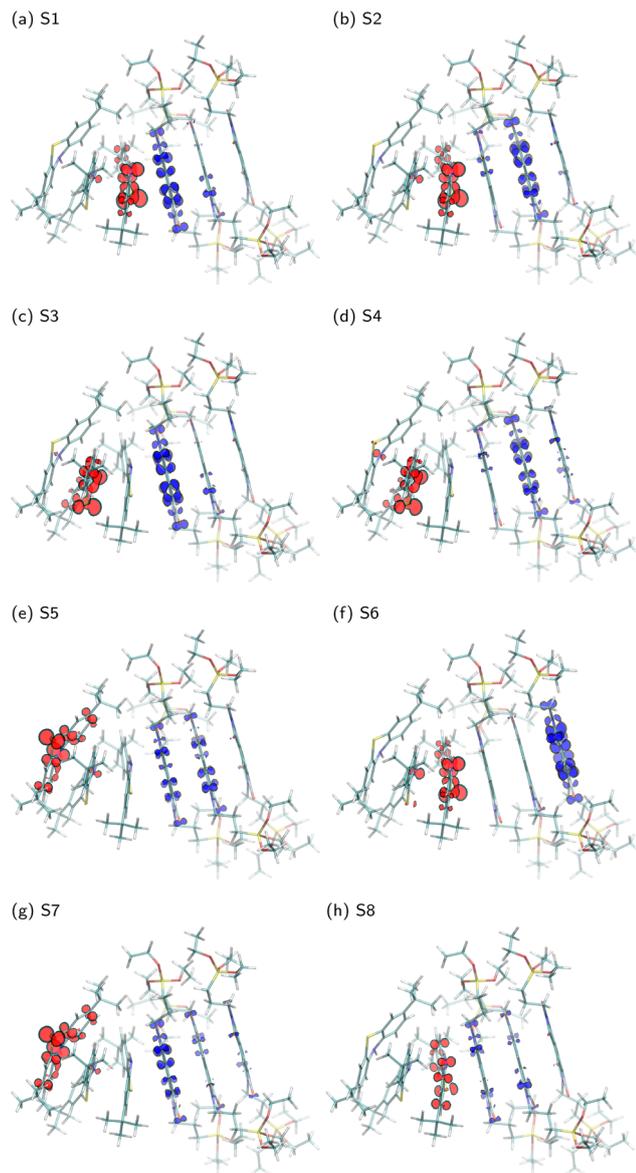
Fig. 3   Difference densities for the first eight excited states, labeled (a)–(h), of the 3-TBP–3-NDI-silane interface model. In all excitations, charge is transferred from the TBP molecules on the left (electron deficient "hole" regions in red; isosurface with isovalue $-0.0002a_0^{-1}$) to the NDI-silane molecules on the right (electron gaining "particle" regions in blue; isosurface with isovalue $0.0002a_0^{-1}$).

electrodes. In the TBP–NDI-silane system the situation is different: The (partial) charge-transfer state is optically active, *i.e.*, carries oscillator strength, and at the same time is the first (lowest in energy) excitation. Thus, the charge-transfer state is not reached from a bright non-charge transfer state *via* a transition of the type that is often described by Marcus theory, but is directly accessed by the optical excitation. This difference is discussed in detail in Section 2.3.3.

For the further process of carrier generation, the electron and hole densities need to decouple, *i.e.*, the exciton binding energy has to be overcome. In Table 2 we report the exciton binding energies for the first eight excitations. They were

calculated as the difference between the fundamental gap as obtained from the frontier eigenvalues of the optimally-tuned range-separated hybrid calculations, and the excitation energies from Table 2. When interpreting the calculated exciton binding energies, the number of molecules explicitly included in the calculation must be kept in mind: our finite-system calculation only includes 3 molecules of each species. In a film, there will be many more molecules, and these can lead to additional dielectric screening. When one takes this effect into account, *e.g.*, *via* a screened range-separated hybrid approach, the exciton binding energy typically is further reduced, and the effect can be substantial, as discussed in detail in ref. 25. Here, we refrain from using a screened range-separated hybrid, as an interface with different electrostatics on each side would be hard to include, and the approach would also introduce empirical elements, *e.g.*, for estimating the effective dielectric constants. Therefore, while it is thus clear that the absolute values for the exciton binding energy that we present here only represent an upper limit, it is encouraging to see that as expected, the exciton binding energies are lower for the higher excitations. This confirms the impression from the visual inspection of Fig. 3, *i.e.*, the higher excited states correspond to electron–hole pairs that are more weakly bound.

The optically active excitations, the multitude of states that exhibit charge-transfer character, and the existence of states in which the electron and hole are well separated offer a promising view on the potential usefulness of the interface for photovoltaic purposes. However, there are also open questions. The first is that the results so far were obtained for one molecular geometry. Further, different geometries should be checked to safeguard against drawing conclusions based on just one geometry that by chance might have particular properties. Second, the energetic ordering of the states, with the most tightly bound exciton lowest in energy, is not ideal for charge separation: if the charge-transfer states in which electron and hole densities are largely separated would be lower in energy than the ones in which they are close together, the excitation would naturally relax into a completely charge-separated state.[20] Changes in geometry and nuclear motion might change the picture or might lead to a coupling of the excitations. Therefore, we examine these effects in the following.

2.3 The 2-TBP–2-NDI interface

2.3.1 Excited states. For studying how nuclear vibrations affect the excited-state energetics, and a more detailed analysis of the interface charge-transfer states, the computational costs need to be decreased considerably. At the same time, however, the important physical characteristics of the model need to be retained. As a first step to reach this goal, we drop the outermost TBP and NDI-silane from the simulation. This leaves us with 2 TBPs and 2 NDI-silanes. As a second step, we replace the silyl residues at the NDIs' endings by methyl residues. This system in the following is designated as 2-TBP–2-NDI. This simplification is justified by the observation that the difference densities in the 3×3 system (*cf.* Fig. 3) show that the electronic excitations predominantly involve the molecules' aromatic

Table 3 Excitation energies and oscillator strength for the first 6 excited states of the 2-TBP–2-NDI system

State	Excitation energy (eV)	O.S.
S1	1.21	0.0576
S2	1.63	0.0001
S3	2.03	0.0020
S4	2.42	0.0006
S5	2.44	0.0243
S6	2.73	0.0007

rings, while the silyl residues play a subordinate role. We optimally tune the range-separation parameter (ω_{opt} = $0.15a_0^{-1}$) for this system and optimize the geometry with ωPBE and a D3 dispersion correction.[51] See the SI for computational details. We calculate the excited states at the geometry-optimized structure to test whether the reduced system reproduces the characteristics of the excited states of the 3-TBP–3-NDI-silane system. Table 3 lists the excitation energies and oscillator strengths of the first 6 excited states, and their difference densities with respect to the ground state are depicted in Fig. 4.

The first excited states of the reduced 2-TBP–2-NDI system show similar charge-transfer character as the excitations in the larger 3-TBP–3-NDI-silane system. All calculated excited states show charge-transfer character, with an electron being transferred from the TBP region to the NDI region. Comparing the difference densities of the 2-TBP–2-NDI system in Fig. 4 with the 3-TBP–3-NDI-silane system in Fig. 3 shows that the same type of molecules is involved. In both cases, the lowest excited state S1 is a charge transfer directly at the interface and with non-negligible oscillator strength. Similarly, S2 and S3 show charge transfers over a larger distance across one rather inactive molecule and even across two rather inactive molecules for S4.

2.3.2 Born–Oppenheimer molecular dynamics. Since organic solar cells are intended to operate at room temperature, nuclear motion has to be taken into account in the excitation analysis. Here, the nuclei are modeled as classical particles that propagate according to Born–Oppenheimer molecular dynamics. We investigate how the adiabatically calculated excited states change along the trajectory and whether their energies overlap. In both the ground-state DFT-based *ab initio* molecular dynamics and the excitation energy calculations, the electrons are treated at the same ωPBE(ω = $0.15a_0^{-1}$) level of theory.

To model realistic structural changes at room temperature, we run Langevin dynamics with the algorithm of ref. 52 at 300 K on the electronic ground state for 2128 fs. Detailed information about the simulation parameters are listed in the SI. Initial conditions for the atom coordinates and velocities are sampled from a Wigner distribution at 300 K. The molecular dynamics are performed within a canonical ensemble.

After *ca.* 0.5 ps the system has reached room temperature and is at equilibrium. We start our analysis from this time onward. Every 4 fs we take a snapshot of the nuclear geometry and calculate the adiabatic excitation energies on that geometry. The resulting excitation energies for the first 4 excited
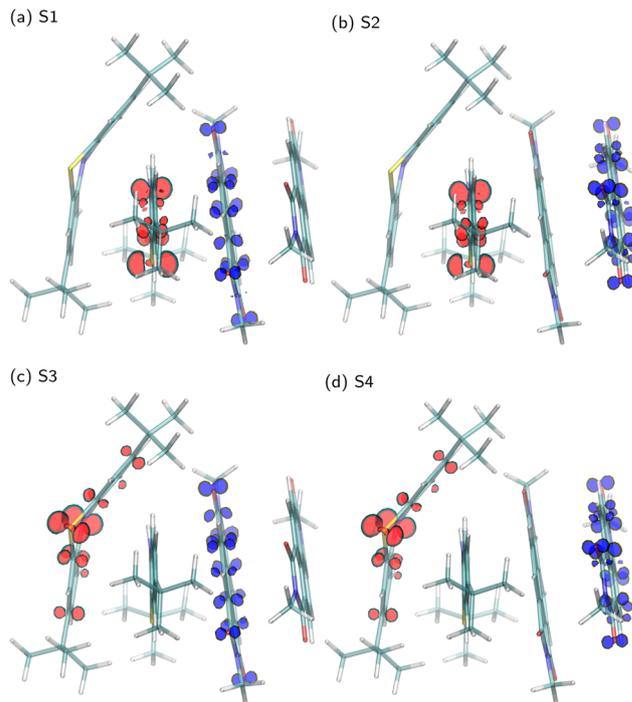

Fig. 4 Difference densities with respect to S0 of S1–S4, labeled (a)–(d), for the 2-TBP–2-NDI system. For all excitations, the "hole" (red isosurface; isovalue $-0.0002a_0^{-1}$) is located in the TBP domain and the "electron" (blue isosurface; isovalue $0.0002a_0^{-1}$) in the NDI domain.

states and the temperature along the trajectory are depicted in Fig. 5. It shows that each excited-state energy fluctuates about half an electron volt along the trajectory. As a consequence of these substantial fluctuations, the different excitation energies get as close as ten millielectronvolts in the course of the simulation.

For clarity, we look at the trajectory data also from a different point of view by presenting a statistical analysis of the excitation energies and oscillator strengths in Fig. 6. The excitation energies and oscillator strengths for all snapshots along the trajectory with their average values are depicted in Fig. 6(a). In Fig. 6(b), the excitation energies are condensed to a probability distribution with a histogram. The decisive insight that emerges from these figures is that the excitation energies clearly overlap. This is particularly well seen in Fig. 6(b) for the excitation energy distributions of S1 and S2. Similar overlaps are observed between S2 and S3, as well as between S3 and S4. Although adiabatic excitation energies do not provide information about the coupling between excited states or population transfer, the observed energetic overlap suggests that excited state population transfer between these states is plausible.

Furthermore, the calculations indicate that the observed electronic states are not specific to the initial geometry but consistently appear across a wide range of geometries, *i.e.*, the (charge-transfer) character of the states is an inherent property of the system. In this context it is also noteworthy to take a look at the oscillator strengths. The mean oscillator strength of S1 is 0.07 and for some molecular geometries along the trajectory the
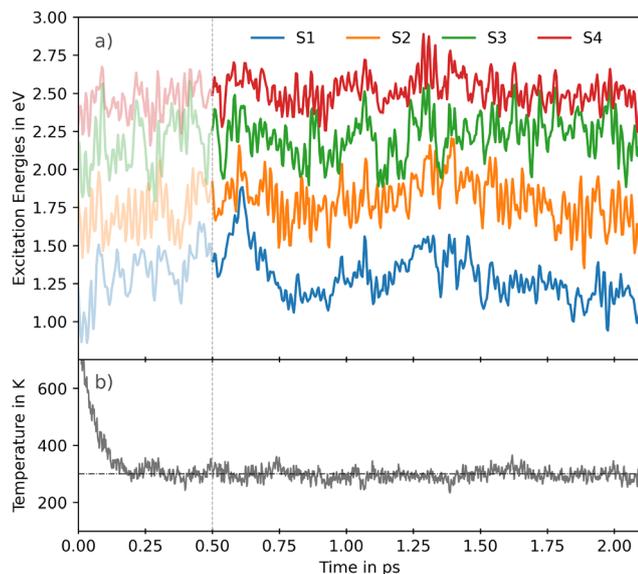
24810 | *Phys. Chem. Chem. Phys.*, 2025, **27**, 24806–24815

This journal is © the Owner Societies 2025

Fig. 5 (a) Adiabatic excitation energies of S1–S4 as function of time along the nuclear trajectory. (b) Instantaneous temperature during the molecular dynamics in dark gray. The horizontal dot-dashed line indicates the thermostat temperature (300 K). The beginning time for the trajectory analysis is marked with a vertical line at 0.5 ps, after which the temperature has stabilized.
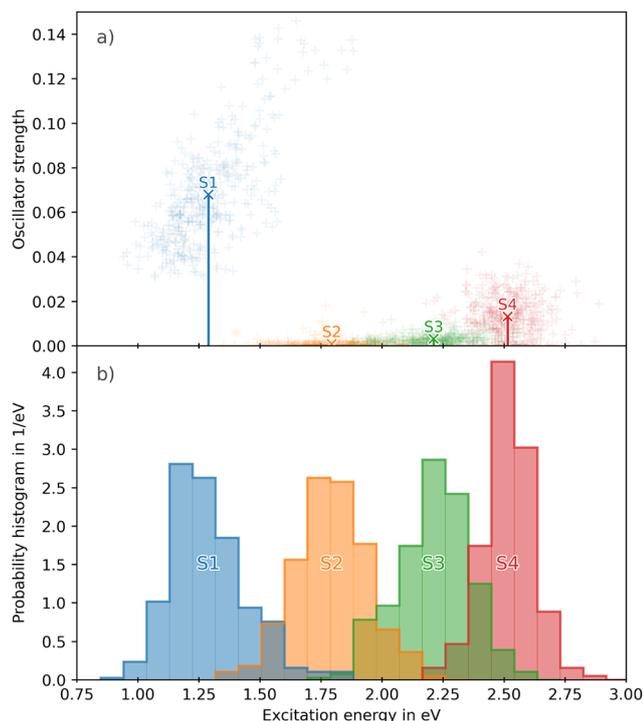

Fig. 6 (a) Excitation energies of S1–S4 with their oscillator strength along the Born–Oppenheimer trajectory. Each "+" marker corresponds to one trajectory snapshot, the average values are depicted with "x" markers and vertical lines. (b) Probability histogram of S1–S4 evaluated from the excitation energies for the molecular structures taken from the Born–Oppenheimer molecular dynamics trajectories.

oscillator strength even reaches values of about 0.14. This average value therefore strongly suggests that this interface excitation is optically accessible under room temperature conditions. A notably weaker optical response is consistently observed for S2–S4. This can be attributed to the increased electron–hole distance, *i.e.*, the reduced overlap of electron and hole orbitals is likely responsible for the reduced intensity of the transitions.

The oscillator strength of S1 together with the indicated coupling to higher states establish a possible pathway for charge separation. After optical excitation of the interface charge-transfer state, nuclear dynamics could drive the transfer to other excited states, leading to the separation of electron and hole. This pathway could be combined with the more traditional pathway of excitation to a higher lying bright state followed by relaxation to lower lying charge-transfer states.

2.3.3 Charge separation and recombination. In this section, we take a closer look at the coupling between the different states of the 2-TBP-2-NDI system that can be involved in the processes of charge transfer, charge separation, and charge recombination. This is motivated by the observation – as already mentioned in Section 2.2 – that the present system differs noticeably from the situation that is typically discussed for molecular donor–acceptor systems:[20] typically, the optical excitation leads to a state in which electron and hole are localized on the same molecular unit. In a second step, this excitation is then followed by a transition to a charge-transfer state, which can subsequently lead to the desired charge separation, or an undesired charge recombination[53,54] The transition is often evaluated using Marcus theory[55–57] or the complementary Marcus–Levich–Jortner (MLJ) theory.[58,59] However, the TBP–NDI system investigated here is characterized by a direct optical excitation of a state with substantial charge-transfer character, *i.e.*, the optically excited state and the charge-transfer state coincide. Furthermore, the system shows a cascade of additional charge-transfer states that are progressively more delocalized and are associated with decreasing exciton binding energies. Therefore, the traditional perspective has to be adjusted.

In order to obtain some first insight into how the charge-separation and charge recombination processes might evolve, we calculate the couplings between different states. The electronic coupling between the states of a donor–acceptor system can be obtained from fragment charge difference (FCD) calculations.[60] In our case, the two TBP molecules define the donor fragment and the two NDI molecules the acceptor. The coupling is obtained from[60]

$$V_{\mathrm{i}\to\mathrm{f}}^{(\mathrm{Qi})} = \frac{(E_{\mathrm{f}} - E_{\mathrm{i}})\Delta q_{\mathrm{if}}}{\sqrt{(\Delta q_{\mathrm{i}} - \Delta q_{\mathrm{f}})^2 + 4\Delta q_{\mathrm{if}}^2}}, \tag{1}$$

where $\Delta q_{\mathrm{i,f}}$ are the donor–acceptor charge differences between the final and initial states and Δq_{if} is the symmetrized off-diagonal donor–acceptor charge population term (see details in ref. 60). The square of the electronic coupling is the quantity that scales the transition between the states in the

This journal is © the Owner Societies 2025

Phys. Chem. Chem. Phys., 2025, **27**, 24806–24815 | **24811**

framework of Marcus theory or, more generally, the Fermi's golden rule.[55–57,61]

For these calculations the geometry that the system assumes in each of the respective states must be known. We show results for the relaxed geometries at the ground state S0 and the first excited state S1, labeled Q0 and Q1, respectively. The Q1 geometry is obtained by finding the energetic minimum of the Born–Oppenheimer surface of the first excited state as calculated by linear-response TDDFT. For reasons of computational practicability, the optimized geometries are calculated with the M06-2X functional, while, for consistency, total energies and excited-state energies are obtained with the ωPBE functional ($\omega = 0.15 \ a_0^{-1}$). For computational details and calculated values see the SI. Obtaining the optimized geometries for higher excited states turns out to be extremely challenging and shows indications of state crossings, and could therefore not be pursued further. However, some of the most relevant insights can already be obtained based on just Q0 and Q1.

Table 4 shows the charge-displacement parameters and the electronic coupling for the transitions of interest as obtained from eqn (1). A first insight gained from Table 4 is that the charge displacements from the donor fragment to the acceptor fragment for the first four excited states are all about 2e, confirming the character of complete charge separation for these states at both the Q0 and the Q1 geometry. Next, we note that the states S2 to S4, which have pronounced charge-transfer character, are relatively well coupled to S1 at the ground-state geometry, with couplings V of about 0.1 eV. Furthermore, S2 and S4 are significantly coupled to S1 at the S1 excited state geometry, with Vs of about 0.3 and 0.6 eV. These high coupling constants indicate that a vibronically mediated interchange between these states[62,63] could be possible. Finally, the last line of Table 4 shows that the coupling for the transfer from S1 (in the excited-state relaxed geometry Q1) back to S0 comes with a coupling of a rather small magnitude, ≈ 0.01 eV. This is a reassuring finding in so far as this transition is associated with charge recombination, $i.e.$, the low coupling here contributes to suppressing the undesired recombination process.

It would be interesting to analyze not only the couplings, but also reorganization energies and transition rates.[64] However, due to the nature of the charge-transfer states in the system, and the size and the complexity of our multi-molecular TBP–NDI system, this is a very challenging task and beyond the scope of the present work. It is reassuring to see, though, that the analysis of the couplings supports the point of view that charge separation can occur at the TBP–NDI interface.

2.4 Experimental insights

As an evaluation of our theoretical predictions, we address the experimental spectroscopic assignment of the charge-transfer states at the interface. Thus, we synthesized the compounds, as described in ref. 35 and 65, and measured their optical absorption. However, measuring charge-transfer states is not straightforward, since it has inherently low oscillator strength in solution and the species responsible for such optical response are only the ones at the donor–acceptor interface. Our approach was to perform vis-NIR absorption measurements in highly concentrated tetrahydrofuran (THF) solutions (30 g L^{-1}), in order to increase the existence probability of TBP–NDI-silane bound species without compromising optical quality (see Methods in the SI).

Fig. 7 (left) shows the THF solution of the single molecules and their 1:2 molar mixture. The solution of the single molecules are transparent. Their absorption bands are only observed above 3 eV ($\lambda > 400$ nm). On the other hand, the mixed solution is light green, showing an absorption band in the red-NIR. Fig. 7 (right) shows the contrast between the NIR-absorption spectrum and the vertical excitations guided by a Gaussian overlap calculated for the 1-TBP–1-NDI-silane configuration. A broad band around 1.8 eV is observed, while the calculated first transition is predicted at 1.46 eV. Considering the large difference between the geometries of dynamic aggregates formed in the concentrated solution at room temperature and the optimized geometry in our calculation, this is a quite reasonable agreement between experimental and calculated data. When comparing experiment and theory here, one
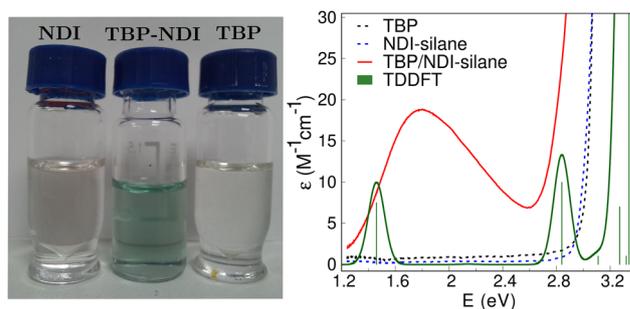
Table 4 Last number in each line: the electronic coupling, $cf.$ eqn (1), for different transitions as indicated by the first entry in each line. The superscript Q0 indicates that the states were calculated based on the geometry optimized in the ground state, whereas the index Q1 denotes states based on the geometry optimized for the first excited state; see main text. The second to fifth number in each line report the parameters that enter eqn (1), where $\Delta E = E_f - E_i$, and i and f refer to the states indicated by the first entry in the line

Transition	Δq_i	Δq_f	Δq_{if}	ΔE (eV)	V (eV)
$S1^{(Q0)} \rightarrow S2^{(Q0)}$	1.960	2.010	−0.007	0.579	−0.078
$S1^{(Q0)} \rightarrow S3^{(Q0)}$	1.960	2.012	0.006	1.076	0.121
$S1^{(Q0)} \rightarrow S4^{(Q0)}$	1.960	2.078	0.008	1.462	0.098
$S1^{(Q1)} \rightarrow S2^{(Q1)}$	1.905	1.928	0.008	1.010	−0.288
$S1^{(Q1)} \rightarrow S3^{(Q1)}$	1.905	1.934	0.000	1.332	0.020
$S1^{(Q1)} \rightarrow S4^{(Q1)}$	1.905	1.872	0.009	1.817	0.572
$S1^{(Q1)} \rightarrow S0^{(Q1)}$	1.905	0.008	0.076	−0.351	−0.014

Fig. 7 (left) Photograph of the THF solutions of TBP, NDI-silane and TBP/NDI-silane 2:1 solutions at a concentration of 30 g L^{-1} (right) and their vis-NIR absorption spectra. Dashed lines are the spectra of the single molecules and the solid red line is the spectrum of the TBP/NDI-silane 2:1 solution. For comparison, TDDFT calculated excitation energies for 1-TBP–1-NDI-silane configuration are presented below the experimental data as green bars and convoluted Gaussian curves.

24812 | $Phys. Chem. Chem. Phys.$, 2025, **27**, 24806–24815

This journal is © the Owner Societies 2025

must also take into account that in the solution on which the experiments are based, aggregates of different sizes and complexity might be forming. This can lead to a distribution of excited states that can contribute to the lowest absorption band. For instance, the contrasts between the lower excited states in Tables 2 and 3 for the 3×3 and 2×2 interface models shows that the excitation spectrum is sensitive to the aggregation.

In order to confirm that the absorption in the NIR region comes from TBP/NDI-silane interfaces, we probed the existence of the long-living TBP/NDI-silane aggregates in the concentrated THF solutions. This was done by dipolar-correlated nuclear magnetic resonance (NMR) spectroscopy using the 1D selective rotating-frame Overhauser effect spectroscopy (1D-ROESY).[66–69] In this technique, a proton species is selectively excited and its magnetic moment transferred through space by dipole–dipole interaction that is averaged out by molecular motion. The resulting spectrum shows the signal due to the selectively excited species plus the ones cross-correlated to the former.[70] In our case, we performed 1D ROESY experiments selectively exciting the aromatic H_3 and H_5 of the TBP (see labeled structure in Fig. S2c), observed close together around 6.9 ppm. As a result, the aromatic protons H_2 of TBP are observed at 6.4 ppm, as expected, and also the ones of the NDI-silane (Fig. S3). This demonstrates that these molecules in THF solution are stacked together transferring magnetization, at least, in the NMR time-scale of milliseconds to seconds. Finally, the compounds and their mixture are stable over many weeks at ambient conditions, either in THF solution or as solid powders, as probed by NMR spectroscopy. The details of the NMR study are described in the SI.

3 Conclusions

In this study, we have investigated the electronic properties of a TBP–NDI interface, a promising system for organic photovoltaics. We found that the lowest excited state, S1, is a charge transfer state at the interface with a favorable excitation energy and oscillator strength. This confirms that this material class has the potential for efficient light-driven charge separation. Higher excited states, S2–S8, also show charge-transfer characteristics with larger electron–hole distances, extending over several molecular units. At room temperature conditions, *ab initio* molecular dynamics simulations showed general optical accessibility of the lowest interfacial charge-transfer state. Furthermore, it revealed energetic overlap between different excited states. We furthermore evaluated the electronic couplings between different states explicitly. In future work, one might think about non-adiabatic simulations that allow for the quantitative analysis of non-adiabatic couplings, *e.g.*, using the methods from ref. 71 and 72. The computational costs of such calculations will be a serious challenge, though. On a qualitative level, the statistical analysis that we presented in the present article can already be seen as a strong hint that coupling between different electronic excitations can be

mediated by nuclear vibrations. This can open a pathway for efficient exciton dissociation. We presented first data on the experimental realization of this material class and a first spectroscopic analysis that is qualitatively in line with the theoretical predictions. Thus, our study confirms the significant potential that the TBP–NDI-silane material class holds for organic photovoltaics.

Author contributions

T. T. ran the calculations of Section 2.1 (partly; geometry optimization and optimal tuning of 2-TBP–2-NDI-silane), Section 2.2 (excited-state calculation on 3-TBP–3-NDI-silane), and Section 2.3 (excited-state calculations and Born–Oppenheimer molecular dynamics of 2-TBP–2-NDI), prepared Fig. 2–6 and Table 1 (partly), 2, and 3, and contributed to the results shown in Section 2.3.3, *e.g.*, *via* excited-state geometry optimizations. R. A. synthesized NDI-silane and performed and discussed the experiments presented in Section 2.4. C. M. I. discussed with T. T. and supervised all TeraChem calculations. S. K. conceptualized the steps of the theoretical approach, structured the analysis of the data, and structured the first manuscript draft. T. B. suggested to study this material combination, initiated the project, did part of the calculations presented in Section 2.1, calculated the couplings in Section 2.3.3, and guided and discussed the experiments discussed in Section 2.4. T. T., S. K., and T. B. together wrote the final manuscript. All authors commented on and discussed the final manuscript.

Conflicts of interest

There are no conflicts to declare.

Data availability

The data supporting this article have been included as part of the supplementary information (SI). Supplementary information is available. See DOI: **https://doi.org/10.1039/d5cp02934a**.

Acknowledgements

This journal is © the Owner Societies 2025

Phys. Chem. Chem. Phys., 2025, **27**, 24806–24815 | **24813**

Notes and references

1 S. Chu, Y. Cui and N. Liu, *Nat. Mater.*, 2017, **16**, 16–22.

2 G. Dennler, M. C. Scharber and C. J. Brabec, *Adv. Mater.*, 2009, **21**, 1323–1338.

3 L. X. Chen, *ACS Energy Lett.*, 2019, **4**, 2537–2539.

4 Y. Cui, H. Yao, J. Zhang, T. Zhang, Y. Wang, L. Hong, K. Xian, B. Xu, S. Zhang, J. Peng, Z. Wei, F. Gao and J. Hou, *Nat. Commun.*, 2019, **10**, 2515.

5 L. Perdigón-Toro, H. Zhang, A. Markina, J. Yuan, S. M. Hosseini, C. M. Wolff, G. Zuo, M. Stolterfoht, Y. Zou, F. Gao, D. Andrienko, S. Shoaee and D. Neher, *Adv. Mater.*, 2020, **32**, 1906763.

6 J. C. Bijleveld, V. S. Gevaerts, D. Di Nuzzo, M. Turbiez, S. G. J. Mathijssen, D. M. de Leeuw, M. M. Wienk and R. A. J. Janssen, *Adv. Mater.*, 2010, **22**, E242–E246.

7 P. R. Berger and M. Kim, *J. Renewable Sustainable Energy*, 2018, **10**, 013508.

8 Y. Li, *Acc. Chem. Res.*, 2012, **45**, 723–733.

9 Y. Lin, J. Wang, Z.-G. Zhang, H. Bai, Y. Li, D. Zhu and X. Zhan, *Adv. Mater.*, 2015, **27**, 1170–1174.

10 L. Feng, J. Yuan, Z. Zhang, H. Peng, Z.-G. Zhang, S. Xu, Y. Liu, Y. Li and Y. Zou, *ACS Appl. Mater. Interfaces*, 2017, **9**, 31985–31992.

11 J. Yuan, Y. Zhang, L. Zhou, G. Zhang, H.-L. Yip, T.-K. Lau, X. Lu, C. Zhu, H. Peng, P. A. Johnson, M. Leclerc, Y. Cao, J. Ulanski, Y. Li and Y. Zou, *Joule*, 2019, **3**, 1140–1151.

12 R. Wang, J. Yuan, R. Wang, G. Han, T. Huang, W. Huang, J. Xue, H.-C. Wang, C. Zhang, C. Zhu, P. Cheng, D. Meng, Y. Yi, K.-H. Wei, Y. Zou and Y. Yang, *Adv. Mater.*, 2019, **31**, 1904215.

13 Y. Cui, H. Yao, J. Zhang, K. Xian, T. Zhang, L. Hong, Y. Wang, Y. Xu, K. Ma, C. An, C. He, Z. Wei, F. Gao and J. Hou, *Adv. Mater.*, 2020, **32**, 1908205.

14 Q. Liu, Y. Jiang, K. Jin, J. Qin, J. Xu, W. Li, J. Xiong, J. Liu, Z. Xiao, K. Sun, S. Yang, X. Zhang and L. Ding, *Sci. Bull.*, 2020, **65**, 272–275.

15 S. Li, L. Zhan, Y. Jin, G. Zhou, T.-K. Lau, R. Qin, M. Shi, C.-Z. Li, H. Zhu, X. Lu, F. Zhang and H. Chen, *Adv. Mater.*, 2020, **32**, 2001160.

16 Y. Shi, Y. Chang, K. Lu, Z. Chen, J. Zhang, Y. Yan, D. Qiu, Y. Liu, M. A. Adil, W. Ma, X. Hao, L. Zhu and Z. Wei, *Nat. Commun.*, 2022, **13**, 3256.

17 S. Liu, J. Yuan, W. Deng, M. Luo, Y. Xie, Q. Liang, Y. Zou, Z. He, H. Wu and Y. Cao, *Nat. Photonics*, 2020, **14**, 300–305.

18 J. Yuan and Y. Zou, *Org. Electron.*, 2022, **102**, 106436.

19 Z.-C. Wen, H. Yin and X.-T. Hao, *Surf. Interfaces*, 2021, **23**, 100921.

20 J.-L. Brédas, J. E. Norton, J. Cornil and V. Corpceanu, *Acc. Chem. Res.*, 2009, **42**, 1691–1699.

21 A. Karolewski, A. Neubig, M. Thelakkat and S. Kümmel, *Phys. Chem. Chem. Phys.*, 2013, **15**, 20016–20025.

22 S. Bhandari, M. Cheung, E. Geva, L. Kronik and B. D. Dunietz, *J. Chem. Theory Comput.*, 2018, **14**, 6287–6294.

23 S. Mahadevan, T. Liu, S. M. Pratik, Y. Li, H. Y. Ho, S. Ouyang, X. Lu, H.-L. Yip, P. C. Chow, J.-L. Brédas, V. Coropceanu, S. K. So and S.-W. Tsang, *Nat. Commun.*, 2024, **15**, 2393.

24 S. Giannini, D. J. Sowood, J. Cerdá, S. Frederix, J. Grüne, G. Londi, T. Marsh, P. Ghosh, I. Duchemin, N. C. Greenham, K. Vandewal, G. D'Avino, A. J. Gillett and D. Beljonne, *Mater. Today*, 2024, **80**, 308–326.

25 S. J. Akram, S. Meißner and S. Kümmel, *Adv. Funct. Mater.*, 2025, 2419236.

26 T. Stein, L. Kronik and R. Baer, *J. Am. Chem. Soc.*, 2009, **131**, 2818–2820.

27 S. Refaely-Abramson, S. Sharifzadeh, M. Jain, R. Baer, J. B. Neaton and L. Kronik, *Phys. Rev. B: Condens. Matter Mater. Phys.*, 2013, **88**, 081204.

28 D. Wing, J. B. Haber, M. R. Filip, S. E. Gant, J. B. Neaton, G. Ohadaan and L. Kronik, *Proc. Natl. Acad. Sci. U. S. A.*, 2021, **118**, e2104556118.

29 M. Brütting, H. Bahmann and S. Kümmel, *J. Chem. Phys. Rapid Commun.*, 2024, **160**, 181101.

30 Z. Chen, Y. Zheng, H. Yan and A. Facchetti, *J. Am. Chem. Soc.*, 2009, **131**, 8–9.

31 A. Karolewski, T. Stein, R. Baer and S. Kümmel, *J. Chem. Phys.*, 2011, **134**, 151101.

32 V. Lemaur, L. Muccioli, C. Zannoni, D. Beljonne, R. Lazzaroni, J. Cornil and Y. Olivier, *Macromolecules*, 2013, **46**, 8171–8178.

33 S. V. Bhosale, M. Al Kobaisi, R. W. Jadhav, P. P. Morajkar, L. A. Jones and S. George, *Chem. Soc. Rev.*, 2021, **50**, 9845–9998.

34 B. Castanheira, E. R. Triboni, L. d S. Andrade, F. d J. Trindade, L. Otubo, A. C. S. C. Teixeira, M. J. Politi, T. B. de Queiroz and S. Brochsztain, *Langmuir*, 2018, **34**, 8195–8204.

35 R. Gabriel de Assis, M. de Oliveira Junior, M. T. Escote, C. B. Pinheiro, J. J. S. Acuña, F. F. Ferreira, L. Sucupira Pedroza, S. Brochsztain and T. B. de Queiroz, *ACS Appl. Eng. Mater.*, 2024, **2**, 1976–1986.

36 S. Kumar, J. Shukla, Y. Kumar and P. Mukhopadhyay, *Org. Chem. Front.*, 2018, **5**, 2254–2276.

37 T. Rodrigues, C. G. d Santos, A. Riposati, L. R. S. Barbosa, P. Di Mascio, R. Itri, M. S. Baptista, O. R. Nascimento and I. L. Nantes, *J. Phys. Chem. B*, 2006, **110**, 12257–12265.

38 Z.-S. Huang, H. Meier and D. Cao, *J. Mater. Chem. C*, 2016, **4**, 2404–2426.

39 R. Grisorio, B. Roose, S. Colella, A. Listorti, G. P. Suranna and A. Abate, *ACS Energy Lett.*, 2017, **2**, 1029–1034.

40 M. Zhai, Y. Miao, H. Wang, L. Wang, X. Ding, C. Chen and M. Cheng, *Dyes Pigm.*, 2022, **202**, 110279.

41 É. G. A. de Miranda, V. H. Toledo, C. G. dos Santos, F. Costa, M. Diaz-Lopez, T. B. de Queiroz, O. R. Nascimento and I. L. Nantes, *J. Photochem. Photobiol., A*, 2023, **444**, 115015.

42 E. Epifanovsky, A. T. B. Gilbert, X. Feng, J. Lee, Y. Mao, N. Mardirossian, P. Pokhilko, A. F. White, M. P. Coons, A. L. Dempwolff, Z. Gan, D. Hait, P. R. Horn, L. D. Jacobson,

24814 | *Phys. Chem. Chem. Phys.*, 2025, **27**, 24806–24815

This journal is © the Owner Societies 2025

I. Kaliman, J. Kussmann, A. W. Lange, K. U. Lao, D. S. Levine, J. Liu, S. C. McKenzie, A. F. Morrison, K. D. Nanda, F. Plasser, D. R. Rehn, M. L. Vidal, Z.-Q. You, Y. Zhu, B. Alam, B. J. Albrecht, A. Aldossary, E. Alguire, J. H. Andersen, V. Athavale, D. Barton, K. Begam, A. Behn, N. Bellonzi, Y. A. Bernard, E. J. Berquist, H. G. A. Burton, A. Carreras, K. Carter-Fenk, R. Chakraborty, A. D. Chien, K. D. Closser, V. Cofer-Shabica, S. Dasgupta, M. de Wergifosse, J. Deng, M. Diedenhofen, H. Do, S. Ehlert, P.-T. Fang, S. Fatehi, Q. Feng, T. Friedhoff, J. Gayvert, Q. Ge, G. Gidofalvi, M. Goldey, J. Gomes, C. E. González-Espinoza, S. Gulania, A. O. Gunina, M. W. D. Hanson-Heine, P. H. P. Harbach, A. Hauser, M. F. Herbst, M. Hernández Vera, M. Hodecker, Z. C. Holden, S. Houck, X. Huang, K. Hui, B. C. Huynh, M. Ivanov, A. Jasz, H. Ji, H. Jiang, B. Kaduk, S. Kähler, K. Khistyaev, J. Kim, G. Kis, P. Klunzinger, Z. Koczor-Benda, J. H. Koh, D. Kosenkov, L. Koulias, T. Kowalczyk, C. M. Krauter, K. Kue, A. Kunitsa, T. Kus, I. Ladjánszki, A. Landau, K. V. Lawler, D. Lefrancois, S. Lehtola, R. R. Li, Y.-P. Li, J. Liang, M. Liebenthal, H.-H. Lin, Y.-S. Lin, F. Liu, K.-Y. Liu, M. Loipersberger, A. Luenser, A. Manjanath, P. Manohar, E. Mansoor, S. F. Manzer, S.-P. Mao, A. V. Marenich, T. Markovich, S. Mason, S. A. Maurer, P. F. McLaughlin, M. F. S. J. Menger, J.-M. Mewes, S. A. Mewes, P. Morgante, J. W. Mullinax, K. J. Oosterbaan, G. Paran, A. C. Paul, S. K. Paul, F. Pavošević, Z. Pei, S. Prager, E. I. Proynov, A. Rak, E. Ramos-Cordoba, B. Rana, A. E. Rask, A. Rettig, R. M. Richard, F. Rob, E. Rossomme, T. Scheele, M. Scheurer, M. Schneider, N. Sergueev, S. M. Sharada, W. Skomorowski, D. W. Small, C. J. Stein, Y.-C. Su, E. J. Sundstrom, Z. Tao, J. Thirman, G. J. Tornai, T. Tsuchimochi, N. M. Tubman, S. P. Veccham, O. Vydrov, J. Wenzel, J. Witte, A. Yamada, K. Yao, S. Yeganeh, S. R. Yost, A. Zech, I. Y. Zhang, X. Zhang, Y. Zhang, D. Zuev, A. Aspuru-Guzik, A. T. Bell, N. A. Besley, K. B. Bravaya, B. R. Brooks, D. Casanova, J.-D. Chai, S. Coriani, C. J. Cramer, G. Cserey, A. E. DePrince, III, R. A. DiStasio, Jr., A. Dreuw, B. D. Dunietz, T. R. Furlani, W. A. Goddard, III, S. Hammes-Schiffer, T. Head-Gordon, W. J. Hehre, C.-P. Hsu, T.-C. Jagau, Y. Jung, A. Klamt, J. Kong, D. S. Lambrecht, W. Liang, N. J. Mayhall, C. W. McCurdy, J. B. Neaton, C. Ochsenfeld, J. A. Parkhill, R. Peverati, V. A. Rassolov, Y. Shao, L. V. Slipchenko, T. Stauch, R. P. Steele, J. E. Subotnik, A. J. W. Thom, A. Tkatchenko, D. G. Truhlar, T. Van Voorhis, T. A. Wesolowski, K. B. Whaley, H. L. Woodcock, III, P. M. Zimmerman, S. Faraji, P. M. W. Gill, M. Head-Gordon, J. M. Herbert and A. I. Krylov, *J. Chem. Phys.*, 2021, **155**, 084801.

43 S. Seritan, C. Bannwarth, B. S. Fales, E. G. Hohenstein, C. M. Isborn, S. I. L. Kokkila-Schumacher, X. Li, F. Liu, N. Luehr, J. W. Snyder Jr., C. Song, A. V. Titov, I. S. Ufimtsev, L.-P. Wang and T. J. MartÃnez, *Wiley Interdisc. Rev.: Comput. Mol. Sci.*, 2021, **11**, e1494.

44 M.-Y. Yeh and H.-C. Lin, *Phys. Chem. Chem. Phys.*, 2014, **16**, 24216–24222.

45 Y. Zhao and D. G. Truhlar, *Theor. Chem. Acc.*, 2008, **120**, 215–241.

46 N. S. S. Kumar, M. D. Gujrati and J. N. Wilson, *Chem. Commun.*, 2010, **46**, 5464–5466.

47 O. A. Vydrov and G. E. Scuseria, *J. Chem. Phys.*, 2006, **125**, 234109.

48 R. Baer, E. Livshits and U. Salzner, *Annu. Rev. Phys. Chem.*, 2010, **61**, 85–109.

49 R. Kroon, M. Lenes, J. C. Hummelen, P. W. M. Blom and B. de Boer, *Polym. Rev.*, 2008, **48**, 531–582.

50 T. M. Clarke and J. R. Durrant, *Chem. Rev.*, 2010, **110**, 6736–6767.

51 S. Grimme, J. Antony, S. Ehrlich and H. Krieg, *J. Chem. Phys.*, 2010, **132**, 154104.

52 G. Bussi and M. Parrinello, *Phys. Rev. E: Stat., Nonlinear, Soft Matter Phys.*, 2007, **75**, 056707.

53 J. Cerdá, J. Calbo, E. Ortí and J. Aragó, *J. Phys. Chem. A*, 2021, **125**, 9982–9994.

54 C. Xiang, Q. Zhao, W. Liu, J. Cao, Y. Zou and H. Zhou, *J. Mater. Chem. A*, 2022, **10**, 25611–25619.

55 R. A. Marcus, *J. Chem. Phys.*, 1956, **24**, 966–978.

56 R. A. Marcus, *J. Chem. Phys.*, 1956, **24**, 979–989.

57 R. A. Marcus, *Rev. Mod. Phys.*, 1993, **65**, 599–610.

58 J. Jortner, *J. Chem. Phys.*, 1976, **64**, 4860–4867.

59 M. Bixon and J. Jortner, *Electron Transfer—from Isolated Molecules to Biomolecules*, John Wiley & Sons, Ltd, 1999, pp. 35–202.

60 A. A. Voityuk and N. Rösch, *J. Chem. Phys.*, 2002, **117**, 5607–5616.

61 M. H. Lee, E. Geva and B. D. Dunietz, *J. Phys. Chem. C*, 2014, **118**, 9780–9789.

62 H. Tamura and I. Burghardt, *J. Am. Chem. Soc.*, 2013, **135**, 16364–16367.

63 Q. Bian, F. Ma and S. Chen, *et al.*, *Nat. Commun.*, 2020, **11**, 617.

64 V. Lemaur, M. Steel, D. Beljonne, J.-L. Brédas and J. Cornil, *J. Am. Chem. Soc.*, 2005, **127**, 6077–6086.

65 A. J. O. Meira, T. B. de Queiroz and A. T. Omori, *J. Braz. Chem. Soc.*, 2025, **36**, e20240153.

66 H. Kessler, H. Oschkinat, C. Griesinger and W. Bermel, *J. Magn. Reson.*, 1986, **70**, 106–133.

67 J. Stonehouse, P. Adell, J. Keeler and A. J. Shaka, *J. Am. Chem. Soc.*, 1994, **116**, 6037–6038.

68 K. Stott, J. Stonehouse, J. Keeler, T.-L. Hwang and A. J. Shaka, *J. Am. Chem. Soc.*, 1995, **117**, 4199–4200.

69 A. Bax and D. G. Davis, *J. Magn. Reson.*, 1985, **63**, 207–213.

70 A. Kumar, R. Christy Rani Grace and P. Madhu, *Prog. Nucl. Magn. Reson. Spectrosc.*, 2000, **37**, 191–319.

71 K. Miyazaki and N. Ananth, *J. Chem. Phys.*, 2023, **159**, 124110.

72 C. A. Myers, K. Miyazaki, T. Trepl, C. M. Isborn and N. Ananth, *J. Chem. Phys.*, 2024, **161**, 084114.

This journal is © the Owner Societies 2025

Phys. Chem. Chem. Phys., 2025, **27**, 24806–24815 | **24815**